vibration

MDPI

Article

Stress Distribution and Transverse Vibration of Flywheel Within Linear Elastic Range

Desejo Filipeson Sozinando *, Kgotso Koketso Leema, Vhahangwele Colleen Sigonde, Bernard Xavier Tchomeni and Alfayo Anyika Alugongo

Department of Industrial Engineering, Operations Management, and Mechanical Engineering, Vaal University of Technology, Vanderbijlpark Campus Private Bag X021, Andries Potgieter Blvd, Vaderbijlpark 1911, South Africa; kgotsol@vut.ac.za (K.K.L.); vhahangweles@vut.ac.za (V.C.S.); bernardt@vut.ac.za (B.X.T.); alfayoa@vut.ac.za (A.A.A.)

* Correspondence: desejos@vut.ac.za

Abstract: Flywheels have been largely used in rotating machine engines to save inertial energy and to limit speed fluctuations. A stress distribution problem is created due to the centrifugal forces that are formed when the flywheel is spinning around, which leads to different levels of pressure and decompression inside its structure. Lack of balance leads to high energy losses through various mechanisms, which deteriorate both the flywheel's expectancy and their ability to rotate at high speeds. Deviation in the design of flywheels from their optimum performance can cause instability issues and even a catastrophic failure during operation. This paper aims to analytically examine the stress distribution of radial and tangential directions along the flywheel structure within a linear elastic range. The eigenvalues and eigenvectors, which are representative of free vibrational features, were extracted by applying finite element analysis (FEA). Natural frequencies and their corresponding vibrating mode shapes and mass participation factors were identified. Furthermore, Kirchhoff–Love plate theory was employed to model the transverse vibration of the system. A general solution for the radial component of the equation of flywheel motion was derived with the help of the Bessel function. The results show certain modes of vibration identified as particularly influential in specific directions. Advanced time-frequency analysis techniques, including but not limited to continuous wavelet transform (CWT) and Hilbert–Huang transform (HHT), were applied to extract transverse vibration features of the flywheel system. It was also found that using CWT, low-frequency vibrations contribute to the majority of the energy in the extracted signal spectrum, while HHT exposes the high-frequency components of vibration that may cause significant structural damage if not addressed in time.

Keywords: stress distribution; transverse vibration; Kirchhoff–Love plate theory; FEA; CWT; HHT

Citation: Sozinando, D.F.; Leema, K.K.; Sigonde, V.C.; Tchomeni, B.X.; Alugongo, A.A. Stress Distribution and Transverse Vibration of Flywheel Within Linear Elastic Range. *Vibration* **2024**, *7*, 1248–1265. https://doi.org/10.3390/vibration7040064

Academic Editor: Ioannis T. Georgiou

Received: 16 October 2024
Revised: 21 November 2024
Accepted: 11 December 2024
Published: 13 December 2024

1. Introduction

The analysis of stress distribution and transverse vibration in flywheels is essential for optimizing their performance in energy storage applications. Flywheels, functioning as kinetic energy storage devices, must endure high rotational speeds and associated stresses while maintaining structural integrity. The centrifugal forces generated during rapid rotation induce stresses in the flywheel, which must be carefully managed to prevent failure. The stress distribution within a flywheel, operating in the linear elastic range, can be thoroughly understood by synthesizing findings from various studies. The stress distributions in a semi-infinite elastic body, influenced by molecular interactions, can be derived from Mindlin's solution, which incorporates a molecular interaction force based on the Lennard–Jones potential [1,2]. This method demonstrates that the stresses acting on surfaces (σ_x, σ_z, and τ_{zx}) depend on the surface distance, where the states of σ_x and σ_z at large distances are equal, and σ_{zx} becomes zero due to the absence of fluctuation [3–6]. In

the context of flywheel operation, inertia is positively correlated with mean concentric linear velocity, and it has been established that this relationship can be employed as a method for load measurement and prescribing individualized training regimens. This relationship is of great importance, as it aids in determining the stress patterns of flywheels under various loads, ensuring that the components remain within the linearly elastic range [7]. Additionally, the study of linear electro-magneto-elastic materials provides insight into the field equations governing such materials and can be employed to investigate the effects of electromagnetic interactions on flywheels [8–11]. Furthermore, it highlights the impact of parabolic temperature distribution on the second-stage deformation of discs composed of nonlinear functionally graded composites modeled using Sherby's law. This underscores the significance of temperature profiles in the distribution of stress and strain rates. For flywheels operating at elevated temperatures, modeling using MATLAB proves particularly suitable for simulating creep behavior and analyzing stress distribution in both radial and tangential directions [12]. In automotive applications, particularly within the powertrain, torsional vibrations are often a significant factor influencing rider comfort. A method of multiple conditions and multiple index assessment has been developed to address these vibrations across various operating modes, including ignition, idle, start, acceleration, deceleration, and transitions between throttle positions. This method evaluates parameters such as the speed amplitude, vibration dose value, peak-to-peak value, vibration isolation rate, and speed fluctuation attenuation rate in dual-mass flywheels (DMFs), both before and after optimization. The optimization process reveals an approximate 7% improvement in the damping effectiveness of DMFs [13]. In spacecraft, the micro-vibration of flywheel rotor systems (SFRSs) becomes a prominent issue. Several studies are being carried out on modeling techniques, suppression methods, isolation, and ground simulation tests to improve the performance of micro-vibration analysis and sensitivity studies [14]. Nonlinear torsional, linear stiffness, and damping characteristics of DMFs have been observed with an increase in the inertia of the primary flywheel. A decrease in the inertia of the secondary flywheel can lower the resonant amplitude and frequency band and obscure other nonlinear dynamic behaviors like quasi-periodic and chaotic vibrations [15]. In the same way, for the three-dimensional vibration isolation in flexible beams, a new approach based on the utilization of the planned motion flywheel assembly has also been developed. This method uses the Lagrange equation and Euler–Bernoulli beam theory and also uses the phase-delay method to control the flywheel's motion. This enabled the beam to be stabilized during free vibration and to minimize displacement in forced vibration, making it more feasible and versatile compared to other conventional boundary control strategies [16–18]. A new efficient algorithm with an application of stochastic resonance (SR) along with wavelet analysis has proven useful in improving the use of noise and identifying the range of orders where fault diagnosis is required under variable speed conditions [19,20]. The power spectral density (PSD) method, along with the Welch method and fast Fourier transform (FFT), were used to analyze the changes in angular velocities and energy variations in flywheel systems. These combinations could clearly show the kinematic response originating from torque pulses [21]. Gray cast-iron flywheels represent one of the most prevalent categories of flywheels utilized in various engineering applications, and a multitude of comprehensive studies have been conducted to meticulously examine the numerous faults and deficiencies that are commonly associated with their performance and functionality. Manufacturing irregularities, such as porosity and microstructural changes, have been identified as key contributors to flywheel failure. To address these challenges and prevent further degradation that could lead to failure, a comprehensive investigation utilizing time-frequency analysis is essential [22]. The integration of time-frequency transformation and data analysis has been found successful in the acquisition of transient data and fault diagnosis of rotating machinery [23]. In most of the flywheel systems, the misalignment and the rotor rubbing are early faults that have been detected using time-frequency analyses such as the smoothed pseudo-Wigner–Ville distributions (SPWVDs). These techniques detect specific super-harmonic and sub-harmonic frequency components that characterize the particular

faults [24–26]. There are mainly two methods, namely empirical mode decomposition (EMD) and the normalized Hilbert transform (NHT), constituting the Hilbert–Huang transform (HHT) in the extraction of features from the multi-component as well as modulated signals. New developments in the HHT, for instance, have seen the development of a soft SSC, which depicts mode-mixing difficulties and improves the modes of decompositions and demodulations, which, in turn, increases the estimation of instantaneous amplitude and frequency [27,28].

In the present work, stress distribution and modal analysis of the flywheel were carried out to determine the effect of stress on the flywheel due to a sudden application of high parametric variation in the speed that substantially increases the centrifugal load. The flywheel is assumed to be homogeneous and isotropic, which is subjected to centrifugal forces due to its rotational motion. Expressions for the governing equations of stress distribution were generated using the assumption of equilibrium of forces and stress–strain relationships. The radial and tangential stress distribution patterns on the flywheel part were analyzed, demonstrating the existence of a proportional relationship between them. FEA was applied to analyze the dynamic properties of the flywheel on the parameters of natural frequencies, mode shapes, and mass participation factors. The procedure included defining the geometry, generating the mesh, using the boundary and loading conditions, solving it using an FEA solver, and post-processing. Material interactive properties and meshing information are also presented, including highlights of the use of SolidWorks and curvature-based meshing techniques. Furthermore, Kirchhoff–Love plate theory was employed to establish the mathematical model governing the flywheel transverse vibration. Bessel functions were used to provide the general solution for the radial component of the equation of motion.

2. Mathematical Formulation of Stress Distribution of Flywheel

By applying the basic laws of solid mechanics and the law of centrifugal forces, the flywheel is assumed to be homogeneous and isotropic, with uniform geometry, mass, and density. The centrifugal force is the primary force that acts on the material of the flywheel that moves through the inertia of the particles of the material when it moves around the axis of rotation. The centrifugal force in a running flywheel causes the particles of the material in question to be subjected to a radial acceleration away from the axis of rotation. These forces set up stresses in the material, which cause deformation if the material is not strong enough to hold such forces.

When examining a circular flywheel of uniform thickness, rotating at an increasing angular velocity around an axis perpendicular to its plane and pivoting about its midpoint, we can regard the thickness of the flywheel as sufficiently small and assume it is primarily under in-plane stress ($\sigma_{ZZ} = 0$). The radial equilibrium equation of the rotating flywheel segment, shown in Figure 1, can be expressed in the following form:

$$\frac{d\sigma_{rr}(r)}{dr} + \frac{\sigma_{\theta\theta}(r) - \sigma_{rr}(r)}{r} + \rho r\left(\omega(t)^2 + \frac{d\omega(t)}{dt}\right) = 0 \quad (1)$$

where ρ stands for the material density of the flywheel, and ω represents the angular velocity as simple harmonic motion (SHM) in the form of $\omega(t) = \omega_{\max}\sin(\omega_f t)$.

In couple stress theory, the radial stress σ_{rr} and circumferential stress $\sigma_{\theta\theta}$ in a cylindrical coordinate system under elastic deformation are derived based on linear elasticity theory. Assuming that both σ_{rr} and $\sigma_{\theta\theta}$ vary with r and that the disk remains within the elastic limit, the stresses σ_{rr} and $\sigma_{\theta\theta}$ in terms of the radial displacement u_r are as follows:

$$\sigma_{rr}(r) = 2\mu\left(\frac{1}{1-\nu}\right)\left(\frac{du_r(r)}{dr} + \nu\frac{u_r(r)}{r}\right) \quad (2)$$

$$\sigma_{\theta\theta}(r) = 2\mu\left(\frac{1}{1-\nu}\right)\left(\frac{u_r(r)}{r} + \nu\frac{du_r(r)}{dr}\right) \quad (3)$$

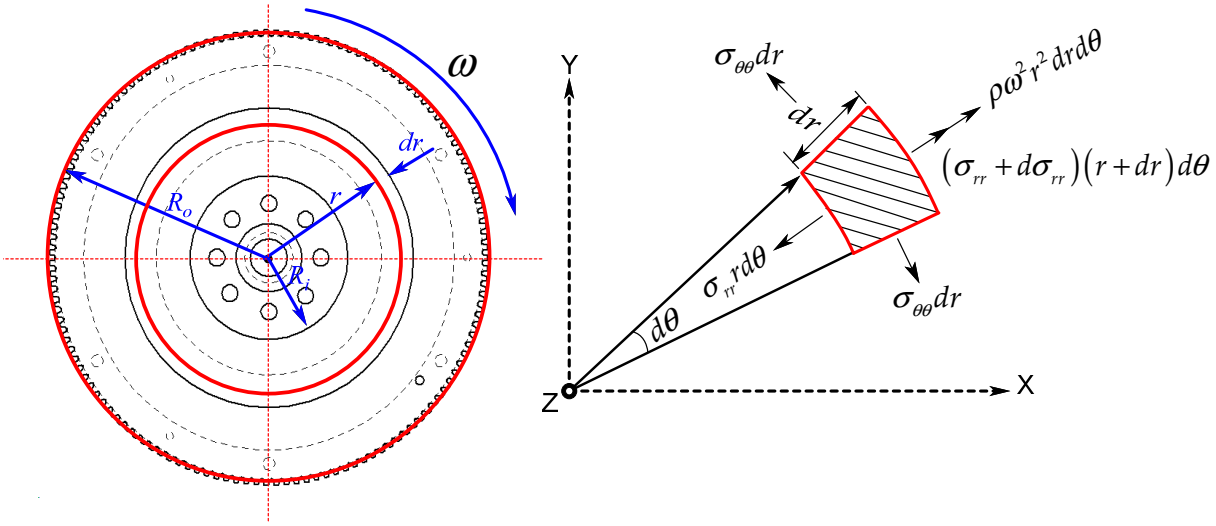

Figure 1. Rotating flywheel and its element.

By considering the annular flywheel with an internal radius R_i and external radius R_o, the boundary conditions are as follows:

Outer radius traction-free: $\sigma_{rr}(R_o, t) = 0$;

Inner radius clamped: $u_r(R_i, t) = 0$.

After applying the boundary condition, the system of Equations (1)–(3) can be solved numerically.

The approximations for the radial stress σ_{rr} and tangential stress $\sigma_{\theta\theta}$ are obtained based on the dominant dynamic terms under the assumptions of high angular velocity. Under dynamic conditions with high angular velocity, the radial displacement $u_r(r)$ is dominated by the forcing term due to the angular velocity ω^2. This forcing term appears as:

$$-\rho r\left(\omega^2 + \frac{d\omega}{dt}\right) \approx -\rho r\omega^2 \tag{4}$$

where ω^2 is much larger than $d\omega/dt$ for steady angular velocity.

The displacement $u_r(r)$ is approximately proportional to r^3 because of the $\rho r^3\omega^2$ term from the inhomogeneous equation.

$$u_r(r) \propto -\frac{\rho r^3\omega^2}{8} \tag{5}$$

$$\frac{du_r}{dr} \propto -\frac{3\rho r^2\omega^2}{8} \tag{6}$$

When we simplify and approximate the dominant term, the radial and tangential stresses can be expressed as:

$$\sigma_{rr} \approx -\frac{\rho r^2\omega^2}{8} \tag{7}$$

$$\sigma_{\theta\theta} \approx \frac{\rho r^2\omega^2}{4} \tag{8}$$

Tresca's yield criterion, also known as maximum shear stress theory, states that yielding starts within the inner radius when the hoop stress is equal to the yield stress available $\sigma_{\theta\theta} = \sigma_{YY}$. This means that if we are to use the yield criterion based on the maximum strain energy incorporated in the maximum shear stress theory, the angular velocity at the onset of yielding is the same as with the von Mises criterion.

$$\sigma_Y^2 = \frac{1}{2}\left[(\sigma_{rr} - \sigma_{\theta\theta})^2 + \sigma_{\theta\theta}^2 + \sigma_{rr}^2\right] \tag{9}$$

The stress is maximum at the inner radius $r = R_i$. After algebraic manipulation of Equation (7), as well as (8) into (9), the angular velocity ω_Y at the initial yielding is given by

$$\omega_Y = \sqrt{\frac{8\sigma_Y}{\sqrt{7}\rho R_i^2}} \tag{10}$$

The parametric analysis of the stress distribution in the flywheel, considering radial and tangential variations, is presented at three different rotational speeds.

The parametric analysis, specifically concerning the radial and the tangential stress patterns of the flywheel element through a range of speeds, is presented in Figure 2. Moreover, a clear dependence is revealed in the form of a similar trend between the radial and tangential stresses versus the radius of the flywheel. Figure 2a shows that the radial stress increases with the increase in the flywheel element radius, where it reaches a critical value at radius r $= \sqrt{\mathrm{R_i R_o}}$, were R_i = 12 mm and R_o = 140 mm, respectively. Moreover, the study depicts the influence of speed on stress distribution. With the increase in flywheel speed, the level of stress in the element also increases. Figure 2b shows complete tangential stress distribution behavior along the flywheel system at different speeds for the max and min stresses at radius $r = R_i$ and $r = R_o$, respectively. The radial stress values are slightly higher at the intermediate radius than the tangential stress, indicating that the radial forces are typically more dominant in the stress field.

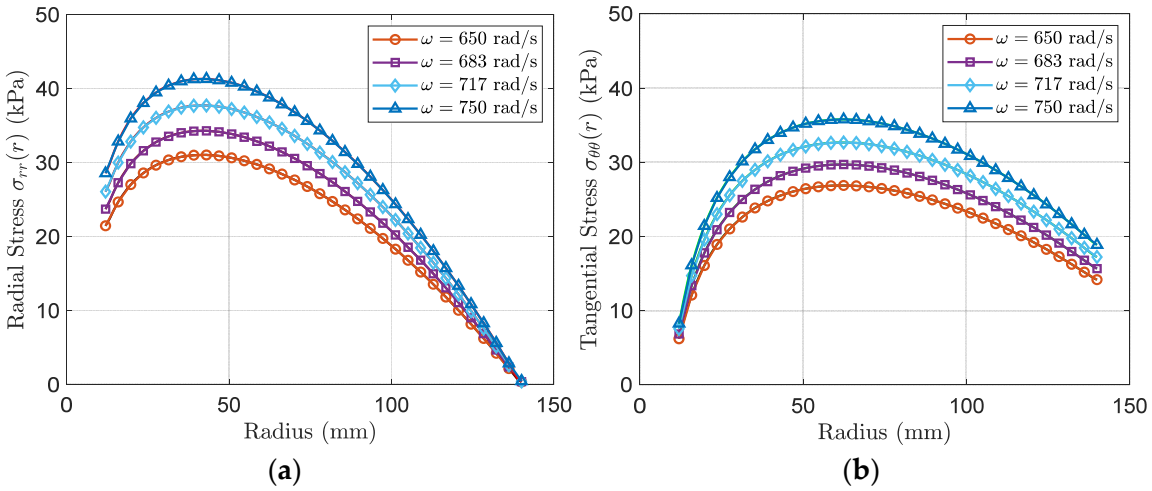

Figure 2. Stress distributions: (**a**) radial variation; (**b**) tangential variation.

Figure 3a presents a correlation between the tangential and radial stress responses and the rotational speed of the flywheel system, characterized by a parabolic relationship. Both tangential and radial stresses increase proportionally with the rotational speed of the flywheel. As the speed increases, so does the stress experienced by the flywheel system in both tangential and radial directions. It is clearly evident that as the rotational speed rises, the stress does not increase uniformly but at an exponential rate, indicating that stress rises rapidly with an increase in speed. The displacement of the flywheel increases proportionally along the inside-to-outside radius, as shown in Figure 3b. This proportionality occurs at the inside radius of the flywheel with minimum displacement until it reaches its maximum displacement at the outside radius of the flywheel. Figure 3b indicates a proportional increase in displacement from the inside to the outside radius of the flywheel. The displacement increases proportionally from the inside to the outside radius of the flywheel, suggesting a consistent pattern of deformation across its radial dimension. This means that as you move from the center towards the periphery of the

flywheel, the amount of displacement experienced by the material also increases. The minimum displacement occurs at the inside radius of the flywheel, gradually increasing until it reaches its maximum at the outside radius. This pattern represents the distribution of stresses in the flywheel at the area near the axis of the flywheel having minimum deformation while the outer rim experiences maximum deformation.

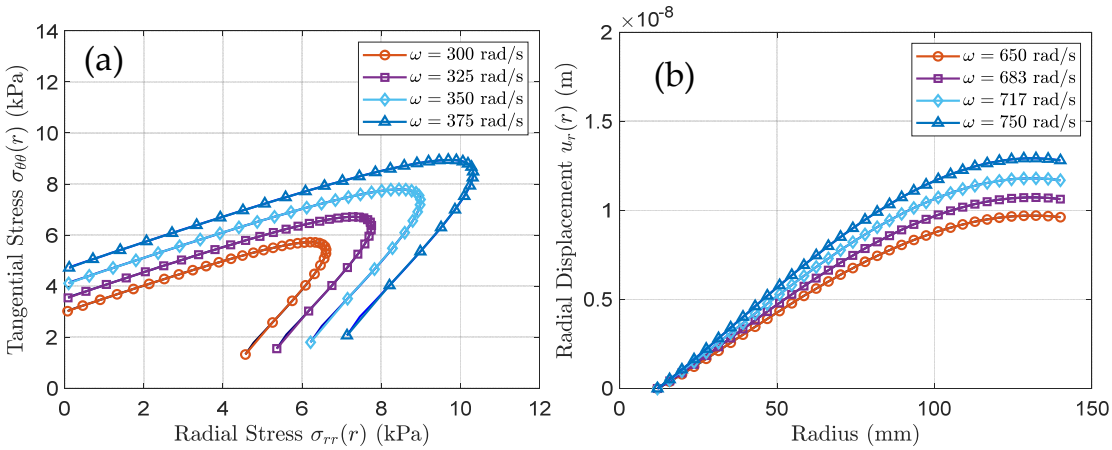

Figure 3. (**a**) Variation in tangential vs. radial stresses; (**b**) displacement along flywheel radius.

3. Finite Element Modal Analysis of Flywheel

Modal analysis is defined as the identification of natural frequencies, damping factors, and mode shapes of the system and the use of these frequency parameters for establishing a mathematical model for the dynamic behavior of the system. The structure of flywheels is divided physically based on frequency and position. The fundamentals of modal analysis are based on the principle that the vibratory response of a single degree of freedom, linear time-invariant dynamic system can be represented as a sum of several simple harmonic motions. They are inherent vibration modes of the dynamic system and are defined exclusively by the physical parameters of the system and their spatial orientation. In each mode, the modal parameters include integral values that define the mode, the natural frequency, and the mode shape. The amplitude of the vibratory response is governed by the characteristics of the exciting force and mode shapes, which, in turn, define the level of various natural modes that are likely to contribute to the system's vibration.

As illustrated in Figure 4, the procedural flow chart pertaining to the FEA simulation is delineated below. This process begins with the input data, which traverses through a series of critical steps in a sequential manner. Initially, it is imperative to delineate the structural geometry of the flywheel alongside its material properties to furnish a realistic representation of the entire system. Subsequently, a mesh generation procedure is executed, which subdivides the intricate geometries into finite elements, thereby facilitating the simulation process. The ensuing step involves the imposition of boundary conditions and loads that emulate real-world scenarios, thereby permitting an evaluation of the structural response in a systematic manner. Throughout the simulation, the FEA solver employs these inputs to yield outputs, which include the natural frequency, mode shapes, and mass participation factors. Post-processing encompasses the determination of the simulation results; this phase involves the scrutiny and interpretation of the deformation modes that may potentially lead to the failure of the flywheel.

In the present instance, SolidWorks was employed to conduct a comprehensive examination of the flywheel structure using finite element methodology, thereby facilitating the simulation and forecasting of mechanical behaviors. Table 1 delineates the properties of the materials that have been incorporated into the finite element analysis for the flywheel structure.

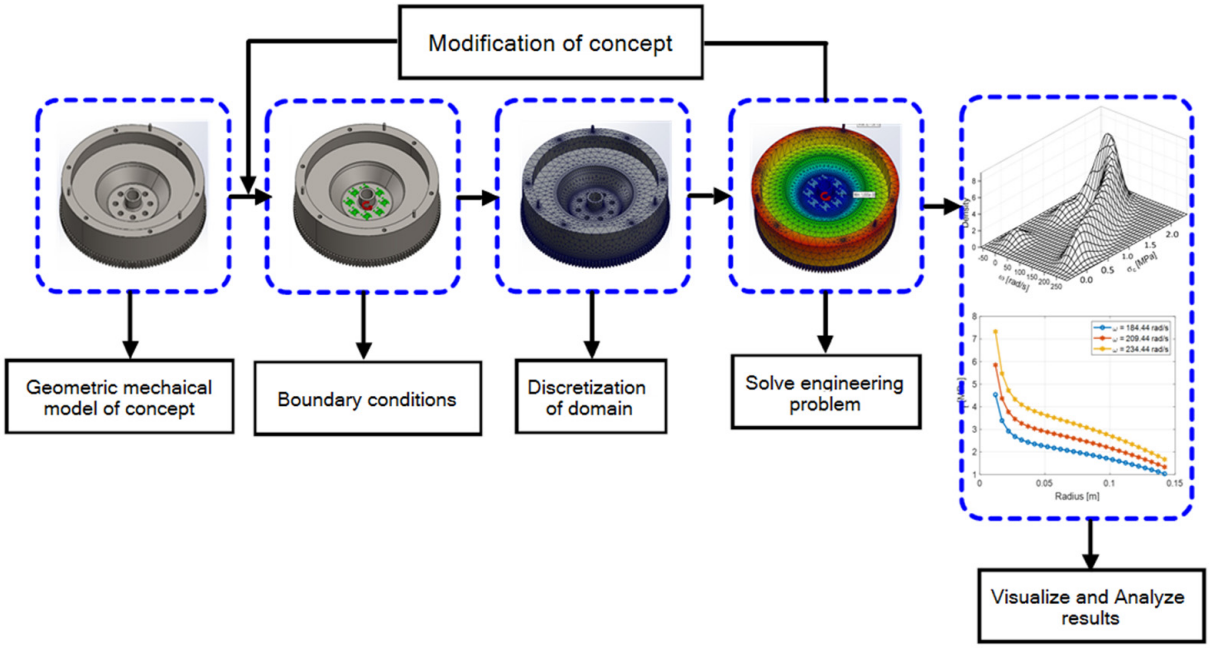

Figure 4. Flowchart of the methodology implied in the FEA simulation.

Table 1. Material properties of the FEA model.

Material	1023 Carbon Steel
Model type	Linear Elastic Isotropic
Failure criterion	Max von Mises Stress
Yield strength	283 MPa
Mass density	7858 kg/m^3
Young's modulus	205 GPa
Poisson's ratio	0.29
Volume	0.0002848 m^3
External diameter	280 mm
Internal diameter	24 mm
Thickness	10 mm

Table 2 presents the specifications related to the meshing techniques employed in the FEA of the flywheel structure. The utilization of the curved-type mesh methodology, which incorporates the geometrical characteristics of the curvatures during the analytical process, signifies the formulation of a mesh possessing smooth edges and precise representations. Jacobian points were used as landmarks to gauge the measure of quality in each mesh using linear tetrahedral elements. An elevation in the maximum element value may correspond with a reduction in computational expenses; however, this correlation concurrently exerts a detrimental effect on accuracy. Conversely, the merits of an enhanced spatial resolution, facilitated by a smaller minimum element size, provide a superior depiction of intricate details and local features, thereby ensuring an accurate representation of the geometric attributes contained within the designated domain.

The vibrational characteristics of the rotational flywheel system are given in Table 3, covering the modes of vibration, the natural frequency of vibration, and the mass participation factor in the X, Y, and Z directions. The table lists the four modes of vibration observed in the flywheel system. Each mode represents a unique pattern of motion in which the flywheel oscillates. For each mode of vibration, the table provides the corresponding natural frequency that represents the frequency at which a system tends to vibrate when excited by an external force without any additional input. The mass participation factor indicates the contribution of each degree of freedom (the X, Y, and Z directions) to a particular mode of vibration. It represents the extent to which the mass of the flywheel participates in

the vibration along each direction. Despite the first two modes having divergent mass participation factors, they engage with a similar frequency, indicating weakly coupled modes of 90° of symmetry between them.

Table 2. Meshing information.

Mesh type	Solid mesh
Mesher type	Blended curvature-based mesh
High-quality mesh based on Jacobian points	16 points
Maximum element size	15.2875 mm
Minimum element size	0.764373 mm
Maximum aspect Ratio	53.254
% of elements with aspect ratio < 3	98.8
% of elements with aspect ratio > 10	0.0525
Quality of mesh	High

Table 3. Mass participation (normalized).

Mode Number	Frequency (Hz)	X Direction	Y Direction	Z Direction
1	600.75	0.00025642	1.3076×10^{-6}	0.020535
2	603.28	0.020639	4.7798×10^{-7}	0.00025695
3	1204	5.7914×10^{-8}	0.45224	2.3186×10^{-7}
4	1477.1	2.3514×10^{-7}	8.1952×10^{-9}	7.4534×10^{-8}
		$\Sigma x = 2.090 \times 10^{-2}$	$\Sigma y = 4.522 \times 10^{-1}$	$\Sigma z = 2.079 \times 10^{-2}$

The outcomes of the simulation results included in Figure 5 describe the first four mode shapes acquired by the finite element modal analysis of the flywheel. The map's representation is given using colors, with red showing the higher intensity of vibration deformation and blue showing a lesser intensity of the vibration deformation. Ideally, each mode shape shows the distribution of the vibration amplitudes of the flywheel structure, where the colors displayed in the maps can be used to differentiate between high and low vibration deformation. The red-colored areas represent the areas where the vibration amplitudes are slightly higher and may be of concern. Some of these regions may suffer higher stress levels and are more likely to fall prone to resonance conditions; hence, this may cause structural failure or damage.

The results presented in Figure 6a depict the waterfall response of the mass participation factor concerning frequency in the X direction. Notably, the graph illustrates a peak mass participation factor of 0.020639 occurring at a resonance frequency of 603.28 Hz, after which the participation factor decreases proportionally with an increase in frequency. This trend suggests a dominant mass involvement in the X direction at the specified resonance frequency, with diminishing influence as the frequency deviates. Similarly, Figure 6b exhibits a proportional increment in the mass participation factor ranging from a minimum to a higher level of 0.45224, observed in the Y direction at a resonance frequency of 1204 Hz. This indicates an increasing dominance of mass participation in the Y direction as the frequency approaches this resonant frequency. In Figure 6c, the maximum peak of mass participation quantified at 0.020535 is observed in the Z direction at a frequency of 600.75 Hz. This signifies a significant contribution of mass participation in the Z direction at this specific resonance frequency.

Figure 7 shows the results of the mass participation factor in different directions and modes of vibration. In the first mode of vibration, only 1.2% of the mass participates, indicating that this mode does not contribute significantly to the overall vibration response in the X direction. However, in the second mode of vibration, a substantial 98.8% of the mass participates. This suggests that the second mode dominates the vibration behavior in the X direction, indicating a higher likelihood of observing significant displacements or responses in this mode. The results also show that 100% of the mass participation occurs in

the third mode of vibration, indicating that the third mode is the critical mode controlling the vibration responses in the Y direction, which shows a strong resonance in this mode. In the Z direction, there is a different pattern of mass participation compared to the X and Y directions. This is whereby the first mode has mass participation represented by 98.8%, meaning a dominant representation in the Z direction. Thus, it can be inferred that the structure or the system would be too sensitive to the vibrations applied in this directive mode in the Z direction. In addition to the above, there is 1.2% of mass participation associated with the second mode and a partial contribution to the mode mentioned above. Interestingly, there is no evidence of mass participation in the fourth mode; this suggests that the contribution of this mode has very little importance in the Z direction.

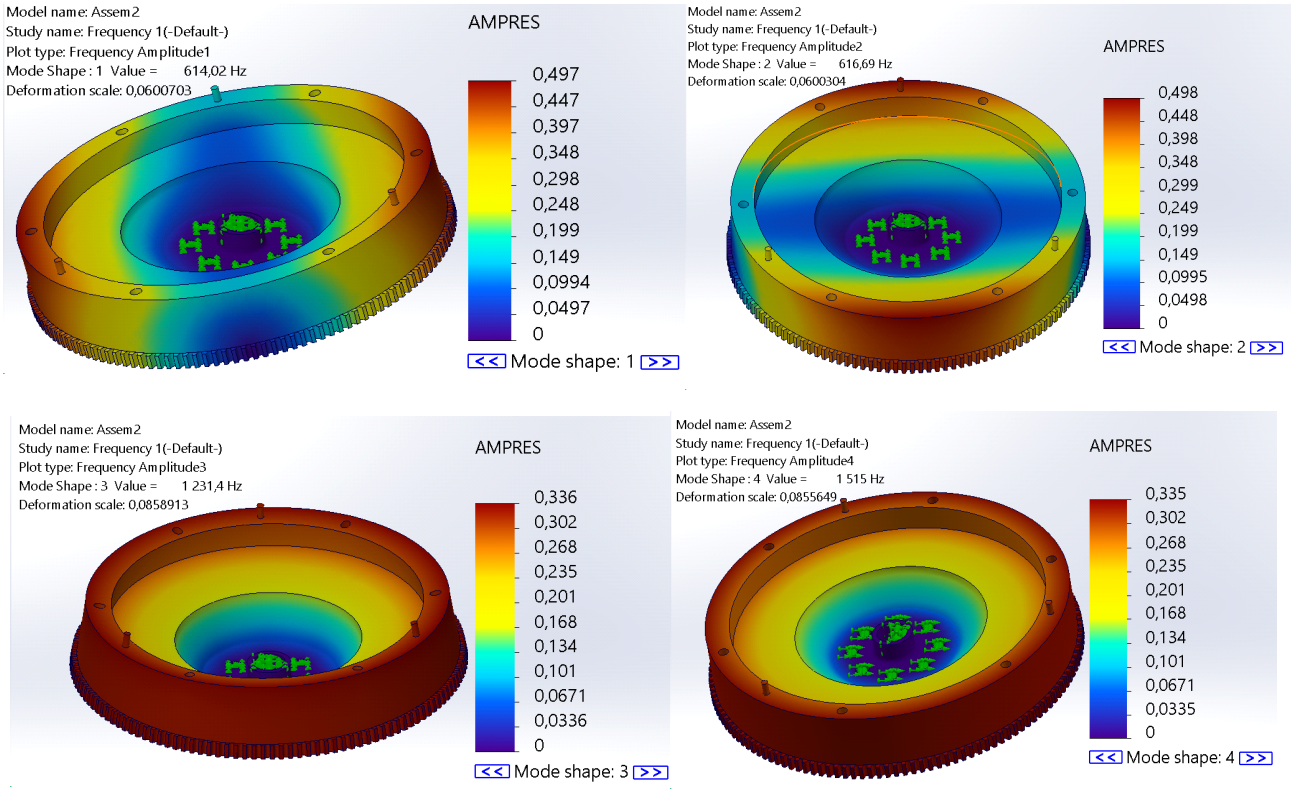

Figure 5. First four deformation modes of vibration.

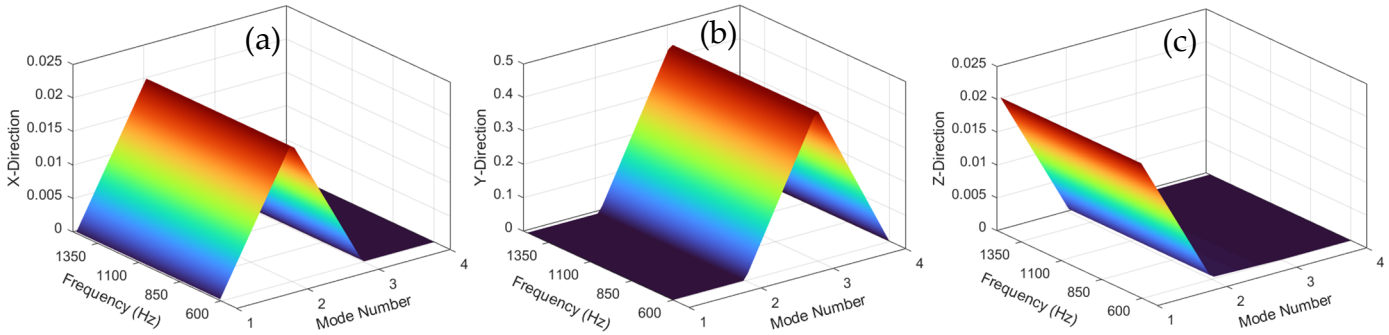

Figure 6. Waterfall response of mass participation factor.

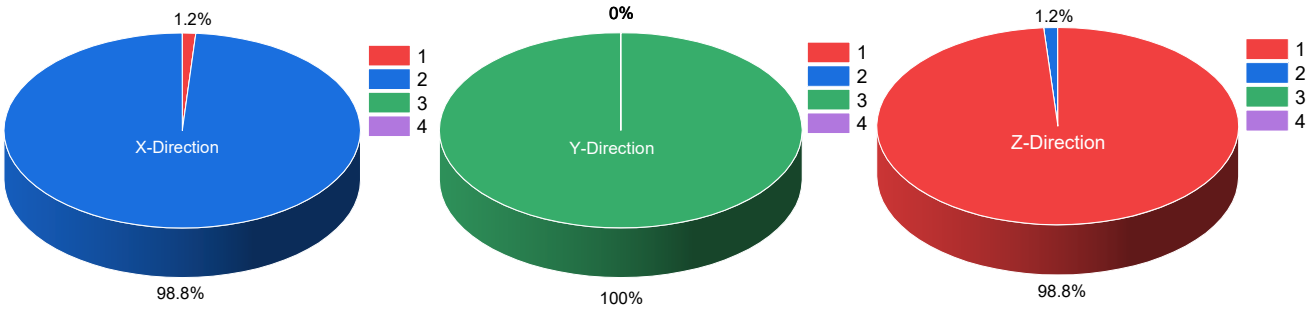

Figure 7. Percentage of mass participation factor in the X, Y, and Z directions.

4. Transverse Vibration Analysis of Flywheel

In this section, Kirchhoff–Love plate theory is applied to model the dynamic motion governing the flywheel system, assuming the following fundamental assumptions to streamline the complex nature of flywheel behavior:

- The cross-sections of the flywheel were originally plane and perpendicular to the mid-surface before deformation and remained plane and perpendicular to the deformed mid-surface after bending.
- The deformations are small enough that the linear approximations of the strains and displacements are valid.
- The flywheel material properties are the same in all directions, and its composition is uniformly distributed throughout.
- The bending moments do not induce in-plane stresses, allowing decoupled analysis of the bending.
- The rotating flywheel is subjected to a small perturbation in the linear elastic range.

The equation governing the transverse vibration flywheel system can be expressed in the following form:

$$\frac{Eh^3}{12(1-\nu^2)}\nabla^4 w + \rho h\frac{\partial^2 w}{\partial t^2} + c\frac{\partial w}{\partial t} = F(t) \tag{11}$$

where h is the thickness of the flywheel, w is the transverse displacement, ∇ is the biharmonic operator, c is the damping coefficient, and $F(t)$ is the random external perturbation force.

$$\nabla^4 w = \left(\frac{\partial^4}{\partial r^4} + \frac{2}{r}\frac{\partial^3}{\partial r^3} - \frac{1}{r^2}\frac{\partial^2}{\partial r^2} + \frac{1}{r^3}\frac{\partial}{\partial r}\right)w \tag{12}$$

Applying the separation of variable method, it can be assumed that a solution occurs in the following form:

$$w(r,\theta,t) = W(r)\Theta(\theta)T(t) \tag{13}$$

Substituting (14) into the governing Equation (12) and separating the variables, the three separate ordinary differential equations can be expressed as:

$$\frac{d^2T}{dt^2} + 2\zeta\omega_n\frac{dT}{dt} + \omega_n^2 T = \frac{F(t)}{\rho h} \tag{14}$$

$$\frac{d^2\Theta}{d\theta^2} + \Omega^2\Theta = 0 \tag{15}$$

$$\frac{Eh^3}{12(1-\nu^2)}\nabla^4 W - \rho h\omega^2 W = 0 \tag{16}$$

By introducing a new variable $k = \sqrt{\frac{12\rho\omega^2(1-\nu^2)}{Eh^2}}$, the general solution for the radial part can be written using Bessel functions:

$$W(r) = AJ_m(kr) + BY_m(kr) + CI_m(kr) + DK_m(kr) \tag{17}$$

where J_m and Y_m are the Bessel functions of the first and the second kinds, and I_m and K_m are the modified Bessel functions of the first and the second kinds. Therefore, the solutions of (15) and (16) can be expressed as:

$$T(t) = [G\cos(\omega_d t) + H\sin(\omega_n t)]e^{-\zeta\omega_n t} + \Gamma \tag{18}$$

$$\Theta(\theta) = E\cos(\Omega\theta) + F\sin(\Omega\theta) \tag{19}$$

where

$$\Gamma = \frac{1}{\rho h}\int_0^t e^{-\zeta\omega_n(t-\tau)}\sin(\omega_d(t-\tau))F(\tau)d\tau \tag{20}$$

The response to random external perturbation Γ is expressed as a convolution integral that accounts for how past perturbations influence the current state of the system.

The boundary conditions are as follows:

1. Clamped at $r = R_1$

$$w(R_i, \theta, t) = 0 \tag{21}$$

$$\left.\frac{\partial w}{\partial r}\right|_{r=R_i} = 0 \tag{22}$$

2. Free at $r = R_2$

$$\left.\frac{\partial^2 w}{\partial r^2}\right|_{r=R_o} + \left.\frac{\nu}{r}\frac{\partial w}{\partial r}\right|_{r=R_o} = 0 \tag{23}$$

$$\left.\frac{\partial}{\partial r}\left(\frac{1}{r}\frac{\partial w}{\partial \theta}\right)\right|_{r=R_2} = 0 \tag{24}$$

3. Symmetry

$$w(r, \theta, t) = w(r, \pi, t) \tag{25}$$

$$\left.\frac{\partial w}{d\theta}\right|_{\theta=0} = \left.\frac{\partial w}{d\theta}\right|_{\theta=\pi} = 0 \tag{26}$$

4. Initial displacement and velocity

$$w(r, \theta, 0) = 0 \tag{27}$$

$$\left.\frac{\partial w}{\partial t}\right|_{t=0} = 0 \tag{28}$$

Substituting (18)–(20), the combined solution can be expressed as:

$$w(r, \theta, t) = [AJ_m(kr) + BY_m(kr) + CI_m(kr) + DK_m(kr)]\Psi\Gamma \tag{29}$$

where $\Psi = [E\cos(\Omega\theta) + F\sin(\Omega\theta)][G\cos(\omega_d t) + H\sin(\omega_d t)]e^{-\zeta\omega t}$

Due to the complexity of (30), the specific constants A, B, C, D, E, F, G, and H can be numerically obtained.

The waveforms for the four normal vibrational modes of the flywheel, depicted in Figure 8a–d, show different modes of deformation at particular natural frequencies. Mode 1 is the first order of oscillation of the flywheel and is the easiest to excite and, thus, the

least energy-consuming. This is because the amplitude indicates that at this fundamental frequency, the flywheel oscillates almost like a harmonic motion. The polar spectrum results in Figure 8e–h illustrate the radial vibrational mode shapes of the flywheel transformed from the normal modes shown in Figure 8a–d, where each mode corresponds to a unique spatial pattern of deformation. As the mode number increases from mode 1 to mode 4, the vibrational energy levels increase with respect to the circumferential positions of the flywheel. This transformation provides radial patterns of the distribution of vibration energy along the radial axis dependent on Bessel functions. In mode 2, the waveform has a greater number of nodes and shows oscillation. Any additional nodes are evidence of a more complex deformation pattern. Such features are observed in the polar plot for mode 2, where, in the second case, there is more fluctuation of amplitude, and clear areas of peak values can be seen. This is an even distribution, which suggests that the vibration is non-uniform and depends more on the angular position phase because specific positions experience higher periodicity of vibrational amplitudes. Mode 3 includes a still more complex waveform, with more oscillations and nodes than the previous modes. The flywheel experiences more complex deformation in that there are many fluctuations within the same angular position. The amplitude stays in the same vicinity while revealing an even higher number of multiple oscillations. Last of all, mode 4 has the largest total number of periodic oscillations of all four modes. This mode possesses the maximum number of nodes and the complex mode of vibration and, thus, represents the maximum deformation of the flywheel.

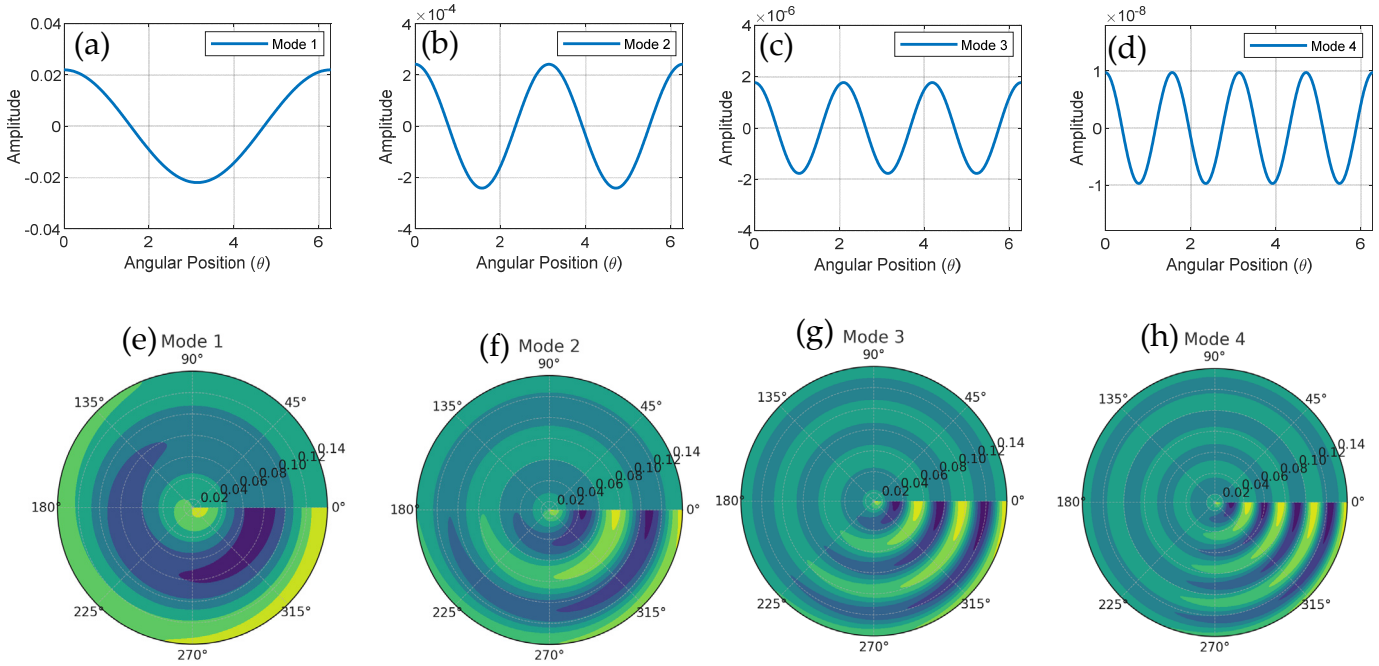

Figure 8. Four normal vibrational modes in waveform and polar spectrum of flywheel.

5. Time-Frequency Analysis of Flywheel

To address the problem of the flywheel vibration signals, a time-frequency (TF) approach is adopted in this section. Hence, it diverges from the conventional Fourier methods, which provide the frequency content of the signal over time. The system parameters for instance, such as the vibrations, are very essential in the flywheel system.

5.1. Continuous Wavelet Transform (CWT)

Continuous wavelet transform (CWT) offers a powerful tool for establishing energy localization over a period represented by a continuous signal or, rather, a time series. It gives a mathematical interpretation of the time-varying parameters of transformations

and positions or separations in order to provide a mathematical model of the dependent multi-scales of the signal. The CWT of a signal $x(t)$ is a general transform that can be expressed mathematically as [29,30]:

$$W_x(a,b) = \frac{1}{\sqrt{|a|}} \int_{-\infty}^{\infty} x(t) \Psi^* \left(\frac{t-b}{a} \right) dt \tag{30}$$

where $W_x(a,b)$ is the wavelet coefficient; $x(t)$ is the input signal; $\Psi(t)$ the mother wavelet; a is the scale parameter, and it dilates or compresses the wavelet; b is a translation parameter and shifts the wavelet; while $\Psi^*(t)$ is the complex conjugate of the mother wavelet.

In Figure 9, the flywheel response is analyzed in terms of vibration from three different angles of view. In this case, the three domains are the time domain, the frequency domain, and the time-frequency domain, each of which exhibits different characteristics of the system. Firstly, the time history of the transverse deflection w of the flywheel is depicted in the time domain over a time of 20 s, as seen in Figure 9a. Secondly, in Figure 9b, it can be seen that the vibration response has FFT frequency components. Also, there is a high amplitude at 1 kHz, thus indicating that most of the vibrational energy is at this frequency. Similarly, the FFT graph shows a lower amplitude at high frequencies up to 20 kHz. This shows that there is a higher frequency but with a low amplitude. Finally, the time-frequency representation is assessed by the CWT spectrum. From the CWT plot in Figure 9c, it is clear that the energy of the signals is more concentrated in low frequencies, with some high frequencies seen at certain time intervals. These are shown through the intensity of the color, with the warmer red indicating a higher frequency at certain moments.

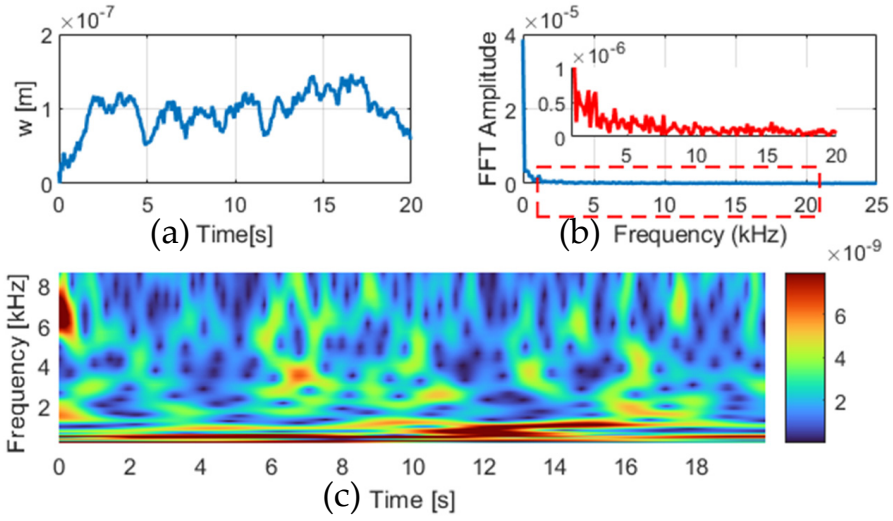

Figure 9. Transverse deflection: (**a**) time domain; (**b**) FFT response; (**c**) CWT spectrum.

The flywheel vibration analysis in Figure 10 shows that the system has low amplitude vibrations, with most of the vibrations occurring at low frequencies. The time-domain signal is displayed in Figure 10a, which shows that there are variations in the signal but with moderate fluctuations. The FFT response provides the same impression of low-frequency vibrations, as seen in Figure 10b. In Figure 10c, the CWT shows that these frequencies remain constant over time, thus indicating the natural behavior of the flywheel in operation. There are no preponderant higher frequency components, which implies that the system is not oscillating at critical or destructive levels.

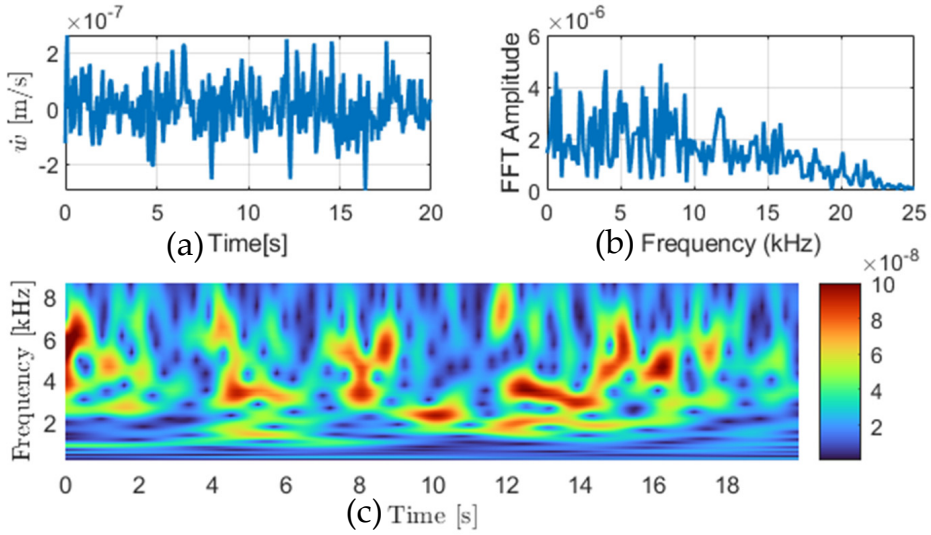

Figure 10. Transverse velocity: (**a**) time domain; (**b**) FFT response; (**c**) CWT spectrum.

5.2. Hilbert–Huang Transform (HHT)

The Hilbert–Huang transform (HHT) is fundamentally structured around empirical mode decomposition (EMD) and Hilbert spectral analysis (HSA). The accurate signal analysis methods that have been used to decompose non-stationary signals are EMD and HSA. EMD is integrated into the HHT, working as the main processing method that decomposes a signal into IMFs that represent the oscillatory modes initially included in the data. These IMFs are derived following a filtration process that locates the oscillatory components with characteristic time scales; this results in a data-adaptive and local formulation of the signal analysis [31].

As mentioned earlier, Hilbert spectral analysis complements EMD by supplying an implicit method for computing amplitude, phase, and instantaneous frequency data of the IMFs. Figure 11 shows a block diagram that allows the analysis of time-varying spectral features inherent in non-stationary signals [32]. However, transverse vibrations can be a serious problem that affects the performance of flywheels, leading to mechanical failures and inefficiencies if their effect is not properly considered. In this section, the signal processing tool, known as the HHT, is applied to analyze the transverse vibration signal of a flywheel and to provide IMFs and IF data.

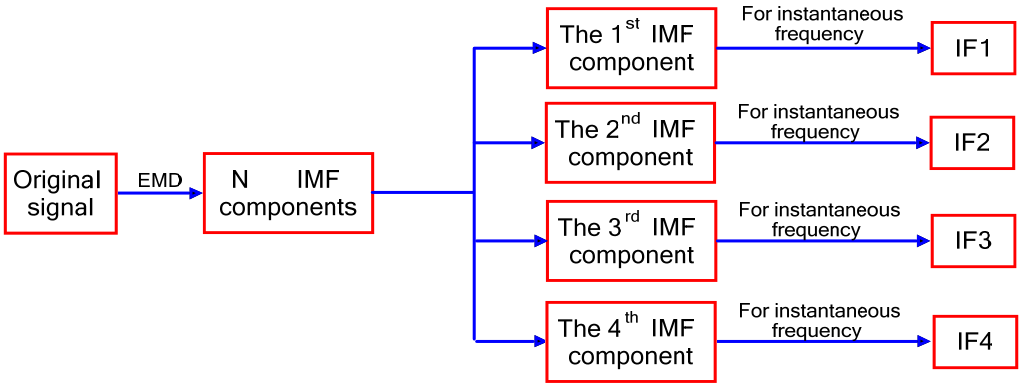

Figure 11. Block diagram of the IF extraction based on HHT.

By applying HHT, the transverse vibration signal of the flywheel is decomposed to reveal the specific characteristics of vibration in various frequency ranges, according to Figure 12. The results show that high-level excitation affects the motion of the flywheel, while more detailed information indicates that the flywheel vibrates tremendously at high

frequencies, which can be tagged as external interferences. These high-frequency vibrations occur in the first IMFs and the respective IFs represent a high frequency of the frequency changes with time. This is why, as the frequency content decreases in the subsequent IMFs, the analysis reveals a more stable and dominant vibrational mode, serving as a predictor of flywheel structural health. However, the lowest-frequency IMF, which has a relatively constant IF, suggests the existence of a critical vibration mode, which will dictate the flywheel's transverse motion.

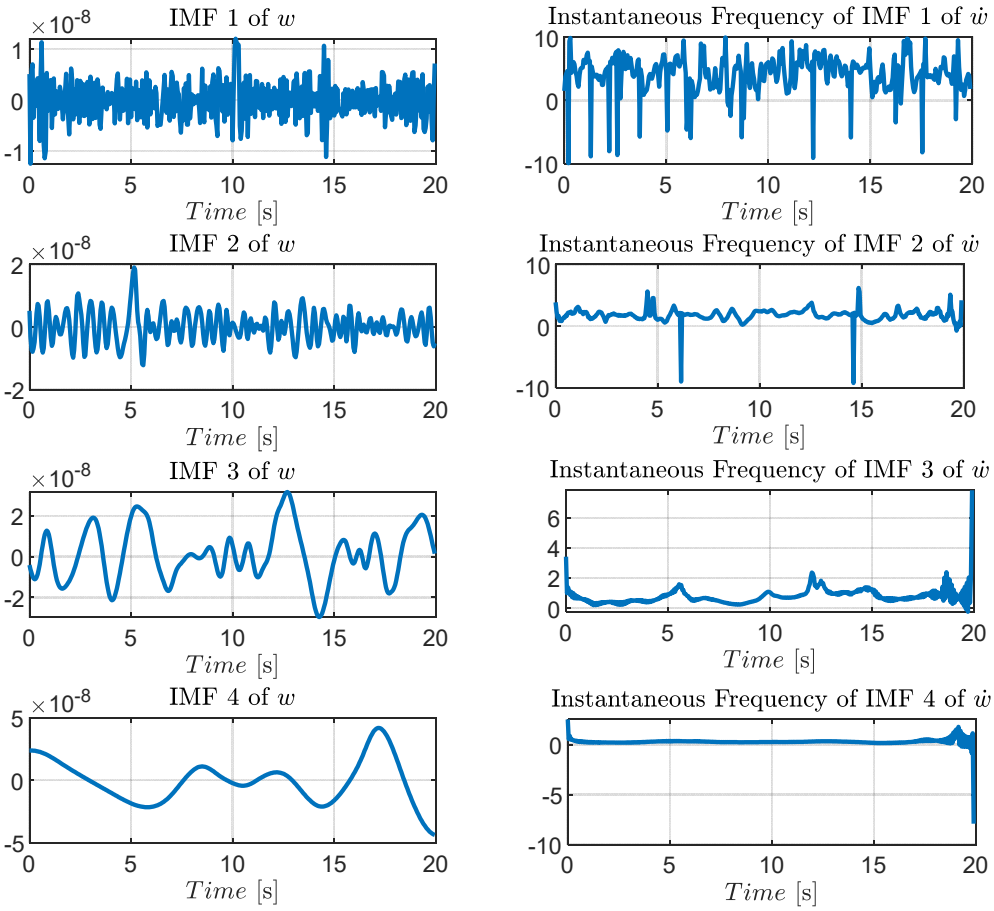

Figure 12. Extraction of IMFs and IF based on HHT.

6. Conclusions

This study has provided a comprehensive analysis of the stress distribution, modal behavior, and transverse vibration of a flywheel operating exclusively within the linear elastic range, using FEA and advanced time-frequency techniques (CWT and HHT). From a stress distribution point of view, major interactions were observed between the radial and tangential stresses, which exhibited a proportional relationship with peak stress at an intermediate radius and then decreased towards the outer radius. This relationship arose due to changes in angular velocity, which caused the peak of radial stress to occur slightly closer to the inner radius, while the peak of tangential stress appeared more evenly distributed between the inner and outer radii. The modal analysis identified the natural frequencies and mode shapes of the flywheel and also provided information on mass participation factors in the X, Y, and Z directions. The results indicated that certain modes dominate the vibration response, particularly in specific directions, causing the dynamic behavior of the flywheel. The transverse vibration analysis, employing CWT and HHT, provided an overview of the time-frequency characteristics of the vibrational behavior of the flywheel. Low-frequency vibrations were observed by CWT analysis and showed an energy density of vibration with higher amplitudes, while the HHT analysis indicated

that high-frequency vibrations could pose a risk of structure failure if not adequately controlled. This current study can be extended to explore the use of advanced materials with higher yield strengths and lower densities to enhance the performance of flywheels while reducing the risk of failure due to stress concentrations. Investigating the impact of thermal effects on stress distribution and vibration behavior would provide a more holistic understanding of the operational dynamics of flywheels and should be supported by experimental benchmarking.

Author Contributions: This study was a collaborative effort between multiple individuals. The topic was conceptualized and initially developed by D.F.S., K.K.L. and V.C.S.; methodology, D.F.S., K.K.L., V.C.S., B.X.T. and A.A.A.; software, D.F.S., B.X.T. and A.A.A.; formal analysis of the data was conducted by D.F.S.; the first version of the manuscript was prepared by D.F.S., K.K.L., V.C.S., B.X.T. and A.A.A.; the manuscript was reviewed and approved by all authors, including D.F.S., K.K.L., V.C.S., B.X.T. and A.A.A. It is also mentioned that the contributions of others were substantial, suggesting that other individuals were also involved in the study but not necessarily listed as authors. All authors have read and agreed to the published version of the manuscript.

Funding: This research received no external funding.

Data Availability Statement: The original contributions presented in the study are included in the article; further inquiries can be directed to the corresponding author.

Acknowledgments: This research study is supported by the Vaal University of Technology, Department of Industrial Engineering, Operations Management and Mechanical Engineering.

Conflicts of Interest: The authors declare no conflicts of interest.

List of Symbols

ρ	Material density
r	Radial distance
$\omega(t)$	Angular velocity
$\frac{d\omega(t)}{dt}$	Angular acceleration
h	Thickness
E	Young's modulus
ν	Poisson's ratio
σ_{rr}	Radial stress
$\sigma_{\theta\theta}$	Tangential (hoop) stress
u_r	Radial displacement
∇^4	Biharmonic operator
c	Damping coefficient
Γ	Response to random external perturbations
k	Wave number
$J_m(kr), Y_m(kr)$	Bessel functions of the first and second kinds
$I_m(kr), K_m(kr)$	Modified Bessel functions of the first and second kinds
Ω	Angular mode number
ζ	Damping ratio
$T(t)$	Time-dependent component
$\Theta(\theta)$	Angular component
ω_n	Undamped natural frequency
ω_d	Damped natural frequency

References

1. Adams, G.G. The contact stress distribution in the receding contact of an elastic layer with a rigid base. *Int. J. Solids Struct.* **2022**, *238*, 111384. [CrossRef]
2. Xiao, S.; Yue, W.V.; Yue, Z.Q. Extended Mindlin solution for a point load in transversely isotropic halfspace with depth heterogeneity. *Eng. Anal. Bound. Elem.* **2023**, *150*, 219–236. [CrossRef]

3. Matsuoka, H.; Otani, T.; Fukui, S. Stress distributions in an elastic body due to molecular interactions considering one-dimensional periodic material distribution based on Mindlin's solution. *Microsyst. Technol.* **2020**, *26*, 139–156. [CrossRef]
4. Wang, Y.W.; Chen, J.; Li, X.F. A deviatoric couple stress Mindlin plate model and its degeneration. *Thin Walled Struct.* **2024**, *200*, 111978. [CrossRef]
5. Ma, S.; Zhang, M.; Ma, L.; Tian, Z.; Li, X.; Su, Z.; Bian, S. Experimental investigation on stress distribution and migration of the overburden during the mining process in deep coal seam mining. *Geoenviron. Disasters* **2023**, *10*, 24. [CrossRef]
6. Hu, W.; Xu, J.; Zhang, W.; Zhao, J.; Zhou, H. Retrieving Surface Deformation of Mining Areas Using ZY-3 Stereo Imagery and DSMs. *Remote Sens.* **2023**, *15*, 4315. [CrossRef]
7. Martín-Rivera, F.; Beato, M.; Alepuz-Moner, V.; Maroto-Izquierdo, S. Use of concentric linear velocity to monitor flywheel exercise load. *Front. Physiol.* **2022**, *13*, 961572. [CrossRef]
8. Amiri-Hezaveh, A.; Karimi, P.; Ostoja-Starzewski, M. Stress field formulation of linear electro-magneto-elastic materials. *Math. Mech. Solids* **2019**, *24*, 3806–3822. [CrossRef]
9. Feng, W.; Yan, Z.; Ma, P.; Lv, C.; Zhang, C. Fracture Mechanics of Magnetoelectroelastic Materials and Structures: State of the Art and Prospects. *Appl. Mech. Rev.* **2024**, *76*, 1–109. [CrossRef]
10. Gan, L.L.; She, G.L. Nonlinear low-velocity impact of magneto-electro-elastic plates with initial geometric imperfection. *Acta Astronaut.* **2024**, *214*, 11–29. [CrossRef]
11. Xu, L.L.; Zheng, Y.F.; Chen, C.P. Nonlinear statics of magneto-electro-elastic nanoplates considering flexomagnetoelectric effect based on nonlocal strain gradient theory. *Thin Walled Struct.* **2024**, *201*, 111974. [CrossRef]
12. Bose, T.; Gupta, K.; Rattan, M.; Chamoli, N. Study of thermal gradation on creep deformation of non-linear varying functionally graded rotating disc. *In IOP Conf. Ser. Mater. Sci. Eng.* **2021**, *1033*, 012084. [CrossRef]
13. Yan, Z.; Nie, H.; Liu, S.; Zhang, B.; Tan, G. Experimental evaluation of the torsional vibration characteristics of a dual-mass flywheel based on multi-condition and multi-index methods. *Proc. Inst. Mech. Eng. D J. Automob. Eng.* **2024**, *238*, 09544070241254598. [CrossRef]
14. Han, Q.; Gao, S.; Chu, F. Micro-Vibration Analysis, Suppression, and Isolation of Spacecraft Flywheel Rotor Systems: A Review. *Vibration* **2024**, *7*, 229–263. [CrossRef]
15. Wei, C.; Niu, H.; Zeng, L. Research on Nonlinear Vibration of Dual Mass Flywheel Considering Piecewise Linear Stiffness and Damping. *Math. Probl. Eng.* **2024**, *2024*, 8683229. [CrossRef]
16. Chu, W.; Wang, Y.Q. Three-dimensional vibration suppression of flexible beams via flywheel assembly. *Aerosp. Sci. Technol.* **2024**, *151*, 109251. [CrossRef]
17. Zhang, L.L.; Huang, J.H. Stability analysis for a flywheel supported on magnetic bearings with delayed feedback control. *Appl. Comput. Electromagn. Soc. J. (ACES)* **2017**, *32*, 642–649.
18. Chu, W.; Wang, Y.Q. Vibration control of a flexible inverted pendulum using the planned flywheel motion. *J. Sound Vib.* **2024**, *569*, 117975. [CrossRef]
19. Wang, B.; Gao, F.; Gupta, M.K.; Krolczyk, G.; Gardoni, P.; Li, Z. RETRACTED: Risk analysis of a flywheel battery gearbox based on optimized stochastic resonance model. *J. Energy Storage* **2022**, *52*, 104926. [CrossRef]
20. Tchomeni, B.X.; Sozinando, D.F.; Alugongo, A. Influences of Hydrodynamic Forces on the Identification of the Rotor-Stator-Rubbing Fault in a Rotating Machinery. *Int. J. Rotating Mach.* **2020**, *2020*, 8816191. [CrossRef]
21. Bueno, Y.P.R.; Soares, R.C. Flywheel sizing and analysis of coefficient fluctuation based on the crank kinematic free response to a torque pulse input. *Aust. J. Mech. Eng.* **2023**, *21*, 1832–1842. [CrossRef]
22. Kar, N. Metallurgical and Mechanical Failure Analysis of an Aftermarket Flywheel. *J. Natl. Acad. Forensic Eng.* **2020**, *37*, 131–137. [CrossRef]
23. Bai, Y.; Cheng, W.; Wen, W.; Liu, Y. Application of Time-Frequency Analysis in Rotating Machinery Fault Diagnosis. *Shock Vib.* **2023**, *2023*, 9878228. [CrossRef]
24. Liu, Z.; Wu, K.; Ma, Z.; Ding, Q. Vibration analysis of a rotating flywheel/flexible coupling system with angular misalignment and rubbing using smoothed pseudo Wigner–Ville distributions. *J. Vib. Eng. Technol.* **2020**, *8*, 761–772. [CrossRef]
25. Zhou, P.; Yang, Y.; Wang, H.; Du, M.; Peng, Z.; Zhang, W. The relationship between fault-induced impulses and harmonic-cluster with applications to rotating machinery fault diagnosis. *Mech. Syst. Signal Process.* **2020**, *144*, 106896. [CrossRef]
26. Wu, W.; Yi, C.; Bai, J.; Huang, Y.; Lin, J. Envelope harmonic noise ratio based adaptive kurtogram and its application in bearing compound fault identification. *IEEE Sens. J.* **2022**, *22*, 8701–8714. [CrossRef]
27. Liu, Z.; Peng, D.; Zuo, M.J.; Xia, J.; Qin, Y. Improved Hilbert–Huang transform with soft sifting stopping criterion and its application to fault diagnosis of wheelset bearings. *ISA Trans.* **2022**, *125*, 426–444. [CrossRef]
28. Khorrami, H.; Sedaghati, R.; Rakheja, S. Vertical Transient Response Analysis of a Cracked Jeffcott Rotor Based on Improved Empirical Mode Decomposition. *Vibration* **2022**, *5*, 408–428. [CrossRef]
29. Cheng, Y.; Lin, M.; Wu, J.; Zhu, H.; Shao, X. Intelligent fault diagnosis of rotating machinery based on continuous wavelet transform-local binary convolutional neural network. *Knowl. Based Syst.* **2021**, *216*, 106796. [CrossRef]
30. Kaji, M.; Parvizian, J.; van de Venn, H.W. Constructing a reliable health indicator for bearings using convolutional autoencoder and continuous wavelet transform. *Appl. Sci.* **2020**, *10*, 8948. [CrossRef]

31. Wang, H.; Ji, Y. A revised Hilbert–Huang transform and its application to fault diagnosis in a rotor system. *Sensors* **2018**, *18*, 4329. [CrossRef]
32. Yu, Z.; Shi, D.; Li, H.; Wang, Y.; Yi, Z.; Wang, Z. An extended kalman filter enhanced hilbert-huang transform in oscillation detection. *arXiv* **2017**, arXiv:1711.04644.